Revealing crystalline domains in a mollusc shell single-crystalline prism

Francesca Mastropietro, Pierre Godard, Manfred Burghammer, Corinne Chevallard, Jean Daillant, Julien Duboisset, Marc Allain, Patrick Guenoun, Julius Nouet, Virginie Chamard

Revealing crystalline domains in a mollusc shell "single-crystalline" prism

F. Mastropietro[1], P. Godard[1†], M. Burghammer[2], C. Chevallard[3], J. Daillant[4], J. Duboisset[1], M. Allain[1], P. Guenoun[3], J. Nouet[5], V. Chamard[1]*

Affiliations

[1] Aix-Marseille Univ, CNRS, Centrale Marseille, Institut Fresnel, Marseille, France.

[2] European Synchrotron Radiation Facility, F-38043 Grenoble Cedex, France

[3] NIMBE, CEA, CNRS, Université Paris-Saclay, CEA Saclay 91191 Gif-sur-Yvette Cedex, France.

[4] Synchrotron SOLEIL, Gif-sur-Yvette Cedex, France

[5] GEOPS, Univ. Paris-Sud, CNRS, Université Paris-Saclay, 91405 Orsay, France

*Correspondence to: V. Chamard, virginie.chamard@fresnel.fr

†Now at: Institut P', CNRS, Université de Poitiers, ENSMA, Futuroscope Chasseneuil, France

Summary

Biomineralization integrates complex processes leading to an extraordinary diversity of calcareous biomineral crystalline architectures, in intriguing contrast with the consistent presence of a submicrometric granular structure. Hence, gaining access to the crystalline architecture at the mesoscale, *i. e.,* over a few granules, is key to building realistic biomineralization scenarios. Here we provide the nanoscale spatial arrangement of the crystalline structure within the "single-crystalline" prisms of the prismatic layer of a *Pinctada margaritifera* shell, exploiting three-dimensional x-ray Bragg ptychography microscopy. We reveal the details of the mesocrystalline organization, evidencing a crystalline coherence extending over a few granules. We additionally prove the existence of larger iso-oriented crystalline domains, slightly misoriented with respect to each other, around one unique rotation axis, and whose shapes are correlated with iso-strain domains. The highlighted mesocrystalline properties support recent biomineralization models involving partial fusion of oriented nanoparticle assembly and/or liquid droplet precursors.

Introduction

Biocrystallisation involves extraordinarily complex and regular biochemical processes whereby living organisms control the crystalline form and texture of their organo-mineral components[1,2]. Only considering calcium carbonate polymorphs in molluscs, corals or sponges, a variety of sub-millimetric structures and shapes are observed, often related to outstanding mechanical properties[1]. These controlled biocrystallization pathways result not only in the synthesis of otherwise unstable crystalline forms but also in hierarchical composite structures with a variety of microstructures, of which mollusc shells are one of the most striking representatives[3]. Different crystalline polymorphs forming various architectures are observed depending not only on the species but also on the precise location within the organism. This latter feature is perfectly illustrated by the famous pearl oyster *Pinctada margaritifera*, which possesses an internal nacreous aragonite layer and an outer prismatic calcite layer[4,5]. The simultaneous crystallization of distinct calcium carbonate polymorphs goes along with very different contents in organic compounds[6], which obviously results in the selection of different nucleation pathways[7].

This architectural diversity at the micro-scale strongly contrasts with the systematic occurrence in calcareous biominerals of crystalline spheroid units[8–10] of apparent diameter in the 50-500 nm range[11], coated by a visco-elastic (likely organic) cortex[8,12], and referred to as granules. In addition, the irregular round shapes of the granules do not provide morphological evidence for a crystalline organization. Nevertheless, the generic characteristic of this sub-micrometric structure, which presents the capability to organize into various micro-scale morphologies, justifies the need of studying the hierarchical arrangement of these sub-micrometric 'building-blocks'. It is foreseen that the understanding of crystallization at this mesoscale level, *i.e.*, over a few granules, is key to building realistic scenarios of bio-crystallization[13].

This issue is repeatedly addressed in the literature, where (indirect) evidences of a mesoscale ultrastructure have been reported, typically in the form of sub-micrometer sized (coherent) crystalline domains. Several bivalve mollusc shells containing many micrometre sized units, which diffract x-rays like single crystals (and are therefore referred to as single-crystal like material)[14–16], present sub-micrometric crystalline domains of coherence lengths in the 250-700 nm range, evidenced by high-resolution x-ray diffraction analysis[14,17]. Domains of comparable sizes were also imaged with 2D transmission electron microscopy[18]. Low mosaicity, in the order of 1° or less between adjacent domains, was noted or inferred in some

biogenic crystals[15,14,19] while largely misoriented crystalline domains (by a few tens of degrees) were observed along the growth direction of mature crystalline units.[5,20,21] Micro-strain fluctuations, in the order of a few 10^{-3} with respect to the mean lattice spacing, were reported as well[14,17,18]. These structural fluctuations (orientations and strains) within the crystal are attributed to the presence of occluded organic molecules.[22,14,17,18] However, a three-dimensional (3D) structural description, which would allow the visualization of the spatial arrangement of those domains, is strongly missing. In this work, we exploit a newly developed x-ray microscopy, 3D x-ray Bragg ptychography, to image the mesoscale crystalline architecture of a *Pinctada margaritifera* calcite prism.

X-ray Bragg ptychography belongs to the so-called coherent diffraction imaging microscopies. These methods aim at retrieving the sample scattering function from a set of coherent intensity measurements, using numerical approaches to determine the phase of the scattered amplitude (not accessible experimentally) and invert it back to real-space[23]. The resulting images contain quantitative sample information, such as material density and/or crystalline displacements, with sub-beam-size spatial resolution. Since the late 90's[24], with the advent of highly-brilliant synchrotron sources, various x-ray methods have been proposed[25]: among these, finite support coherent diffraction imaging and Fourier-transform holography have been largely exploited, either in the forward scattering regime[26,27] or in the Bragg geometry[28,29]. X-ray Bragg ptychography, inspired by electron beam ptychography[30] and combining approaches arising from Bragg coherent diffraction imaging[31] and x-ray (forward) ptychography,[32,33] has been recently proposed for the 3D imaging of extended crystalline material structured at the nanoscale.[34–36] It takes advantage of the weak interaction of x-rays with matter, allowing for structural investigations of a sample without specific preparation. In the forward direction, *i. e.*, in the vicinity of the reciprocal space origin, the sensitivity of x-ray ptychography is exploited for imaging the 3D density of materials such as amorphous biominerals[37]. In Bragg diffraction conditions, the internal periodicity of the crystalline lattice produces highly intense Bragg peaks that contain information on the crystal properties of a given crystal plane family[36,38]. A Bragg ptychography measurement consists in recording a set of 3D Bragg diffraction intensity patterns, resulting from the interaction between a finite-sized coherent beam and the investigated object under Bragg conditions. From the data set, a phase retrieval algorithm reconstructs numerically the 3D sample map, which provides detailed information on the sample crystalline properties, such as crystalline coherence, relative strain field and relative crystalline plane rotation, imaged with a spatial

resolution of few tens of nanometers.[36] The high-sensitivity of this crystalline microscopy allows one to distinguish crystalline domains with lattice mismatch of a few 10^{-4} and/or presenting misorientations of a few 10^{-2} degree. In the context of the biomineralization question, the unique capabilities of x-ray Bragg ptychography represent assets allowing one to shed new light on the mesoscale crystalline organization.

Results

Our study was performed on the outer layer of a juvenile *Pinctada margaritifera* border shell (Fig. 1). This organism was selected owing to the well-known apparent simplicity of its calcitic prisms, each prism being described as a homogeneous single-crystalline like material (Supplementary Figure 1), at least during the early stage of the prism growth[39]. The prism assembly displays a rather homogeneous orientation of the crystal lattice *c*-axis, which lies roughly perpendicular to the prism surface, while the in-plane crystalline orientation varies from one prism to the other. Some of the specific morphologies observed at different length scales of the shell are shown in Figs 1A-D. At the shell border, where the thickness is estimated to 0.5-2 μm[5], the calcite prisms are easily recognized with a typical lateral size of 30 μm, surrounded by their organic envelopes (Fig. 1B-C). The presence of disks - the preliminary form of prisms - only visible at the very border of the shell, confirms that the earliest stages of the prismatic growth are present in our sample[5]. In apparent opposition with the prism crystalline homogeneity, atomic force microscopy in tapping mode (phase lag) emphasizes, with a nanoscale resolution, the existence of a granular structure, which is composed of rounded mineral units with apparent sizes estimated here to about 50-200 nm (Fig. 1D). At slightly larger length scales, 3D images obtained with CARS (coherent anti-Stokes Raman scattering) microscopy, a non-linear 3D optical microscopy method sensitive to chemical bond vibrations (here the crystalline carbonate vibration mode) evidences spatial fluctuations of crystalline carbonate density, with visible homogeneity along the prism thickness (Supplementary Information and Supplementary Figure 2).

The 3D x-ray Bragg ptychography experiments were performed on a prism selected in the vicinity of the preserved growth edge, using the experimental set-up of the ESRF ID13 beamline, schematically depicted in Fig. 2 (see also Methods). The sample, located on a translation and rotation stage, is illuminated by a nano-focused beam (Supplementary Figures 3 and 4) under Bragg conditions, so that a given Bragg reflection can be investigated in details (Fig. 2A, B). The chosen prism region is probed by shifting the sample transversely to the beam along two translation directions, t_x and t_y. The Laue geometry employed here, which

gives access to a Bragg reflection in transmission, allows minimizing the beam footprint on the surface, a condition that has been found to be of major importance for the successful reconstruction of this complex material. The chosen 110 reflection probes the lattice planes that are almost perpendicular to the prism thickness (Fig. 2B). The detailed characteristics of the 3D intensity distribution produced by the illuminated volume are investigated by scanning angularly the sample with respect to the incident angle ω, over an angular range of about 2° (Fig. 2C and Supplementary Figure 5). In this way, the 2D far-field intensity patterns successively extract information along the direction perpendicular to the Bragg vector. The patterns are finally assembled to produce a 3D intensity volume, corresponding to a finite 3D extent of the crystal reciprocal space, for each illumination position (Fig. 2D). While a single 3D diffraction intensity pattern encodes 3D information on the sample structure at a length scale possibly smaller than the beam size, the whole set of spatially-dependent 3D intensity patterns has to be simultaneously phased back[34,40] to provide the 3D structural image over the whole illuminated sample volume (see Methods). Note that the finite extents of the spatial and angular scans (translation and rocking curve) impose that only a limited spatial field of view is imaged and that only the crystal components that meet the Bragg conditions are probed. Consequently, one has to keep in mind that the final image is a spatial truncation of the sample, which possibly exhibits some empty parts that would correspond to misoriented crystalline regions.

The retrieved 3D images are shown in Figs. 3 and 4. They feature a region close to the prism center, schematically represented in Fig. 3A. The envelope of the full retrieved volume is shown as a yellow-grey surface. Its finite extent along the prism surface reflects the equally limited extent of the illuminated volume according to the measurement modalities, while along the third direction ($\approx \mathbf{z}$), the limit corresponds to the prism thickness, estimated to about 1.75 μm (see Methods and Supplementary Figure 6). The Bragg ptychography reconstruction returns a complex-valued function whose phase (φ) holds information on the crystalline properties[31,34,41]. This retrieved phase φ, which is directly proportional to the displacements of the (110) crystalline planes, was therefore further analyzed: its spatial derivatives are related to the tilt and strain of the (110) crystal planes (see Pateras *et al*.[36] and Methods). Both tilt and strain present abrupt spatial variations, revealing that even at this early growth stage, the crystal is not (strictly speaking) single-crystalline but is composed of several iso-oriented domains, slightly tilted with respect to one another, and of several iso-strain domains, slightly strained with respect to the mean lattice parameter. Concerning the rotations, we unexpectedly

observe that the iso-oriented domains display a strongly anisotropic tilt distribution, over an angular range of about 1.2 degree, which occurs solely around a single rotation axis, named δ and found to be almost collinear to **y,** an axis that lies along the prism surface (Fig. 3B). We note that this anisotropic rotation distribution obtained from the reconstruction is in agreement with the peculiar shape of the Bragg intensity, which presents a linear spread perpendicular to the mean 110 Bragg vector direction (Fig. 2D). On the contrary, an isotropic distribution of the crystal plane tilts, around a mean direction, would result in a Bragg vector distribution describing a cone on the Ewald sphere. A series of 2D cross-sections through the rotation map is shown in Fig. 3B. The visualization of the 3D spatial arrangements of the iso-oriented domains, in Figs. 3B, D-G, is facilitated with a surface color rendering, where each iso-oriented domain external surface is drawn using a color that encodes its respective rotation angle, according to the color-scale of Fig. 3B. The discrepancy observed between the retrieved volume shape and the illuminated cylindrical volume, indicates some missing parts in the probed region. Most likely, these correspond to misorientations, which could not be captured owing to the limited amplitude of the rocking curve. The same image analysis has been made on the strain map, which evidences iso-strain domains of total strain amplitude ε of about 2.5 10^{-3} (Fig. 3H-K). For both tilt and strain domains, a striking result is the elongated shape of the iso-oriented and iso-strain crystalline domains that extend all along the prism thickness (Fig. 3E,I). In the transverse direction, where the apparent extent of the domains is artificially limited by the experimentally accessible field of view, the domain transverse size is estimated at least to about 400 nm. Finally, the 3D visualization of both strain and rotation maps makes possible the comparison between the iso-oriented and iso-strain domain shapes, which exhibit some strong but partial correlations: while one of the iso-oriented domains (in *blue*) fully corresponds to one of the iso-strain domains (in *orange*), the large iso-oriented domain (in *orange*) is actually composed of two different iso-strain domains (in *blue* and *green*). The third tiny iso-oriented domain (in *green*) appears as part of one of the last iso-strain domain (in *green*).

In addition to the crystal plane tilt and strain, the phase that is retrieved with the 3D Bragg ptychography reconstruction allows the visualization of the crystalline coherence within the iso-oriented domains (see Methods). The 2D maps plotted in Fig. 4 correspond to 2D cuts through the distribution of the retrieved φ, extracted solely for the iso-oriented domain of Fig. 3D. The abrupt changes in the colored representation of φ correspond to a phase shift of about 4.2 rad, *i. e.*, a displacement of 0.16 nm (or 2/3 of the (110) lattice spacing), located at the

transition between the iso-strain domains of Fig. 3I and J. They evidence the existence of a finite coherence length, which manifests itself as an iso-color area, with typical dimensions of about 400 nm.

A second ptychography reconstruction, which corresponds to an investigation performed within the same prism, in a region nearby the one shown here (Supplementary Figure 7) exhibits similar crystalline features: spatial distribution of crystal plane tilt and strain, single (and same) rotation axis, extent of the iso-oriented and iso-strain domains over the prism thickness and finite crystalline coherence length. In complement to these 3D microscopy analyses, an incoherent x-ray micro-diffraction set-up was used to perform an extended spatial investigation of the 006 Bragg peak, on the whole area of another prism (Supplementary Figure 3). The obtained 3D intensity patterns, which were found to be systematically elongated along a fixed direction (over an angular range of about 1°) confirms the existence of the distribution of crystal plane tilts around a single rotation axis, whose direction is contained into the (**xy**) plane, that is the prism surface. These microdiffraction results are in full consistency with the ptychography reconstruction.

Discussions

The produced ptychography images result from the inversion of a single Bragg reflection, whose extent was restricted by the limited signal dynamics. Therefore, the 3D images detail structural information on the 110 crystalline planes only, with mesoscale spatial resolution. This implies that local imperfections of the crystalline lattice, *i. e.*, near the atomic level (vacancies, inclusions), cannot be resolved and that the full strain tensor is not accessible. We note that the later one is not an intrinsic limit[25] and significant resolution improvements are to come thanks to the on-going advent of several extremely brilliant synchrotron sources, which should deliver increased coherent flux and allow for improved measurement strategies.[42] A first conclusion drawn from the presented experiments is the confirmation of a mesoscale arrangement of the granules into larger crystalline domains. The herein 3D images of the crystalline properties allowed us to identify two typical length scales: (*i*) a shorter one, of about 400 nm (*i. e.* larger than the granule size) corresponding to the typical size of the coherent crystalline domains, in agreement with previous observations on several species[14,17,18,43] and (*ii*) a second one, most likely slightly larger, corresponding to the extent of domains which exhibit the same crystalline plane tilt and strain (the iso-oriented and iso-strain domains). We note that mosaicity of comparable angular spread (about or less than a degree) was already measured in thick, *i. e.* older, biogenic marine crystal units.[14,15,19]

Comparable micro-strain fluctuations (in the order of a few 10^{-3}) have already been reported as well.[14,17,18] The presence of a crystalline mosaicity and strain distribution, already observed at the most early growth stage of the prisms, indicates that structural disorder is a core part of the growth mechanism. The additional and new information that is brought with this work concerns the spatial organization of those sub-micrometric domains, a step forward made possible by the Bragg ptychography microscopy. In some of our observations (Figs. 3E,I,J and Supplementary Figure 7), the iso-oriented and iso-strain domains clearly expand over the whole prism thickness, which is the prism growth direction according to the model of layered growth mode[10,44]. The orientation distribution (or rotational disorder) of the calcite planes presents a clear anisotropic behavior, with the rotation occurring around a single axis, contained into the prism surface. Moreover, the rotation axis direction is constant all over the prism. We note that the existence of the rotation axis and the determination of its direction, that requires the 3D measurement of the Bragg diffraction pattern (with coherent or incoherent x-rays) has not been evidenced previously, to the best of our knowledge. Finally, the similarity between the iso-oriented and iso-strain domain shapes demonstrates a common origin of these structural features, although the latter do not fully correlate in space.

The structural information that we are bringing along provides new elements that have to be accounted for in the calcareous biomineralization scheme, a question that we briefly discuss in the following. At large length scale, recent results indicate that the growth of the prismatic structure (prisms size and shapes) may originate from simple physical effects, related to grain growth theory.[45] On the contrary, at the nano and meso-scales, it is generally accepted that calcareous biominerals, and more specifically mollusc shells, cannot be produced within the classical crystalline nucleation and growth scheme, owing to their mesocrystal structure (nanoparticle assembly)[13] and to the likely occurrence of an amorphous precursor, which would explain the observed round granules and molten morphologies[46]. Based on bio-inspired syntheses and micro-structural observations, several bio-crystallization scenarios have been proposed, some of which are consistent with our observations. The observed iso-oriented and iso-strain domains of assembled granules could be explained by a mesocrystal formation scheme, which involves colloidal organic-mediated arrangement of crystalline nanoparticles of common crystallographic orientation.[47] The iso-strain domains could be induced by the presence of previously observed occluded organics molecules, as seen in biogenic[18,48] and synthetic biomaterials.[49] Additionally, the proposed oriented attachment of crystalline primary nanoparticles during mesocrystal formation[47] can preserve the crystalline coherence between

nanoparticles if they fuse together. Mesocrystalline growth could therefore agree with our observations in *Pinctada* prisms, of coherent crystalline domains larger than the granule size, as well with other reported observations[14,43]. However, the round shape of the granules suggests a slightly different mechanism where mesoscale structuring occurs through an assembly and subsequent crystallization of amorphous particles[50]. An attractive scenario has been currently developed, in which these solid amorphous granules result from the solid transformation of a liquid precursor, the so-called PILP (polymer induced liquid precursor) process[46]. Such a scenario would explain the observed crystalline coherence by the propagation of a crystallization front through the inter-connected granules and would agree as well with the likely absence of porosity in our structural reconstruction (observed at least in the limit of our resolution level, Supplementary Figure 8). Note that this scenario would also be consistent with TEM observations performed on another calcareous biocrystal[10]. Finally, our observations of a reduced rotational disorder, both in disorder dimension (observation of a single rotation axis, contained in the prism plane) and in disorder amplitude (no rotation observed along the prism thickness) calls for a specifically oriented growth mode. Extrinsic preferential orientation can be invoked, through the growth along organic fibers[51] or sheets[52], for instance, while the fluctuations in the organic molecule density could produce strain fluctuations within the same iso-oriented domains[17,18]. A gradual shift in orientation of the crystal lattice has been reported in films produced by PILP, attributed to dehydration shrinkage stresses during crystal solidification constrained by the substrate[53]: similar effects could be at play during the uniaxial growth of the prism. These could be confirmed by the detailed investigations of the rotational disorder spatial evolution, as a function of the distance to the crystallization centers, if any[5]. It is remarkable, that the herein observed rotation axis (*i. e.*, the rotational disorder axis) lies in the growth layer plane[44]. The possibility to conclude on a definite biomineralization mechanism, at least for *Pinctada* prisms, would certainly require additional structural investigations involving a larger field of view. Future works will aim at identifying and investigating regions near the mineralization fronts, where we expect to observe structural differences with respect to the two models. Indeed, assuming that the regions near the mineralization front correspond to a not fully completed crystallisation process, one may expect the coherence domains to be of smaller extent than the crystalline domain for the oriented-attachment model while the crystalline coherence should scale with the size of the crystalline domain, for the liquid-like precursor model. Still, our 3D description of the crystalline architecture brings a set of new arguments in favor of recently reported models, namely the oriented attachment and partial fusion of a mesoscale assembly scenario[47]

and the PILP intermediate model[54], which both appear able to account for the herein observed complexity of the mesoscale arrangement of the granules produced by biomineralization.

Conclusions

To conclude, we have revealed the complexity of the crystalline biomineral at the mesoscale, by providing a 3D spatial description of the crystalline network with a nanometric resolution. The wealth of information that we brought with this recently developed imaging method demonstrates that new findings on the understanding of the biomineralization process are within reach.

Methods

Sample preparation. The juvenile *Pinctada margaritifera* shells were grown at the IFREMER hatchery at the biological station of Taravao-Vairao (Tahiti). They were cultivated in an optimal and controlled sanitary environment to avoid any contamination during growth. Once selected, they were preserved in ethanol/sea-water solution and transferred to the geology laboratory in Orsay (France). Before the x-ray experiment, they were cut into small pieces of about 1 mm^2 and glued on the top of a metallic tip. This process ensures the integrity of the investigated part of the shell is preserved.

X-ray Bragg diffraction experiments. The x-ray Bragg diffraction experiments were performed at the ID13 beamline of the European Synchrotron Radiation Facility. The monochromatic coherent beam of wavelength λ (energy bandwidth $\Delta\lambda/\lambda \approx 10^{-4}$) was focused down to the sample position (see Supplemental Information). The sample, fixed on a metallic tip was mounted onto a three-axis piezo-electric stage, itself placed on the top of a hexapod. The laboratory frame (x,y,z) was defined with respect to the sample surface: **x** and **y** are along the prism surface, with **y** along the shell growth direction, and **z** is perpendicular to the prism surface. The sample was translated into the focal plane of the lenses, using an optical microscope with a 1 μm depth of focus. A 2D Maxipix (486 x 516 pixels, 55 μm width) detector was placed on a trail, allowing the adjustment of the diffraction angle and detector-to-sample distance. The 3D diffraction patterns were built by stacking the 2D intensity patterns obtained while scanning the incidence angle ω along the so-called "rocking curve", in step of $\delta\omega$. The beam-to-sample position was adjusted by translating the sample along the t_x and t_y directions.

For the ptychography experiment, the beam was tuned to 15 keV (λ = 0.83 Å), illuminating a set of crossed silicon refractive lenses of 25 μm effective aperture and 0.01 m focal length. A pair of slits was placed in front of the lenses in order to restrict the illumination area. Its aperture was set to 40 x 60 μm^2 along the horizontal (H) and vertical directions (V), respectively, ensuring fully spatially coherent illumination. Before the sample investigation itself, a full characterization of the complex-valued illumination function was performed[35]. The transverse beam size at the sample position was hereby estimated to 0.08 x 0.1 μm^2 (H x V, full width at half-maximum). For the shell imaging, the Bragg ptychography experiment was performed in Laue geometry on the transmitted 110 calcite diffraction peak, where the transmission geometry was chosen in order to minimize the beam footprint on the sample. For this diffraction angle, the longitudinal coherence condition across the sample is ensured up to a sample thickness of about 1.9 μm. This condition is verified in our experiment where the prism thickness has been estimated to 1.75 μm (from both scanning electron microscopy and reconstruction results, see Supplemental Information). The diffraction signal was collected at a Bragg angle $2\theta_B$ of 19.2° while the detector-to-sample distance (2.6 m) ensured that coherence and sampling conditions are fulfilled. The five-dimensional ptychography data set was obtained by recording the 2D intensity patterns while scanning the sample across the beam (along t_x and t_y) with steps of 45 nm. It provides an overlapping of approximately 70% between two successive positions of the 9 x 9 point mesh. This strong spatial redundancy is needed to ensure the convergence of the phase retrieval inversion process. After each mesh, the incidence angle ω was modified ($\delta\omega$ = 0.007°) before a new mesh was performed. A total of 286 points along the rocking curve was needed to cover the whole Bragg diffraction peak

extent (about 2°). The acquisition time, limited to 0.8 s per frame led to a maximum of intensity of approximately 30 photons/pixel. In total, the acquisition time, including motor motions, electronic reading of the detector and data transfers, took 9 hours corresponding to a total illumination time of about 5.2 hours. For the reconstruction shown in the Supplemental Information, the whole scan was slightly reduced: the rocking curve was limited to 230 points and the acquisition time was limited to 0.5 s per frame. The whole scan took approximately 4.7 hours for a total illumination time of 2.6 hours.

For further analysis, the 3D intensity patterns were registered as a function of the momentum transfer $\mathbf{q}$, where $\mathbf{q} = \mathbf{k}_f - \mathbf{k}_i$ and $\mathbf{k}_{i,f}$ is the incident (resp., exit) wave vector ($|\mathbf{k}_{i,f}| = 2\pi/\lambda$). A relevant 3D frame for $\mathbf{q}$ is given by the detection frame (q_1, q_2, q_3), where q_1 and q_2 are along the detector plane (q_1 being additionally contained in the diffraction plane) and q_3 is aligned the rocking curve direction.

The Bragg micro-diffraction experiments (further detailed in the Supplemental Information) were performed in Bragg geometry on the same set-up as the one used for ptychography, during a different beam time. The 12.36 keV incoming radiation ($\lambda = 1$Å) was impinging onto a partially illuminated Fresnel zone plate focusing element, resulting in a focal spot size of 0.3 x 0.2 μm^2 (H x V, full width at half-maximum). The Bragg diffraction patterns were collected in the vicinity of the 006 calcite Bragg reflection ($2\theta_B = 20.2°$), in a reflection geometry, leading to an elongation of the beam footprint onto the sample up to 1.7 x 0.2 μm^2. The detector was placed 2 m away from the sample position. The 3D patterns were collected with $\delta\omega = 0.1°$ over the prism area, using translation steps of 5 and 1 μm along **x** and **y**, respectively.

3D Bragg ptychography phase retrieval. The inversion of the five-dimensional data set was performed with our 3D Bragg ptychography algorithms adapted from our 2D development[40]. In order to preserve the signal information, the phase retrieval algorithm was directly performed in the detection frame, which is non-orthogonal and results in defining a non-orthogonal direct space obtained from Fourier conjugation relations[35]. The final 3D image was transferred into the orthogonal laboratory frame.
The inversion was performed with an optimized procedure, extensively tested on noisy numerical data, mimicking as much as possible the experimental conditions (probe, sampling, scanning, intensity dynamical range, *etc.*), and detailed in the Supplemental Information. All along, the error-metric derived from a Gaussian likelihood was used to account for the photonic shot noise in the intensity measurements. A regularization term was introduced in the criterion in order to favor thickness-limited solution. The thickness of the shell sample was first refined directly from the inversion method. Indeed, we observed on numerical tests, that the lower error metric value corresponded to the best agreement between the regularization thickness and the true shell thickness. This was obtained with 100 cycles of ordered-subset algorithm iterations, initiated with a sample structure of random values (amplitude and phase). The best agreement was found for a sample thickness of 1.75 μm. Once the regularization thickness was optimized, 100 cycles of truly converging conjugated gradient algorithm were run, resulting in the presented reconstructions.

Image analysis. The 3D complex-valued solution resulting from the inversion process is the sample scattering function ρ, which for a crystal can be expressed by[41]

$$\rho = |\rho| \exp(i\varphi)$$

where the phase φ is related to the crystalline properties through

$$\varphi = \mathbf{G}_{110} \cdot \mathbf{u}$$

with **u** the crystalline displacement field and $\mathbf{G}_{110}$ the Bragg vector of the investigated reflection ($G_{110} = 2.525\ 10^4\ \mu m^{-1}$). Hence, the knowledge of φ gives access to the projection u_{110} of the displacement field onto the Bragg vector. From this quantity, one can access several crystalline properties. As an example, with respect to crystalline coherence, u_{110} is continuous in a coherent crystalline domain, while it presents a change (*e. g.*, a shift) in the vicinity of a crystalline defect. Furthermore, the crystalline plane rotations around the two directions perpendicular to $\mathbf{G}_{110}$ can be extracted directly from the derivative of u_{110} with regards to these two axes. In the same way, the derivative of u_{110} with regards to the coordinate collinear to $\mathbf{G}_{110}$ gives access to a relative strain ε (derivations of the complete expressions can be found elsewhere[36]).

For all investigated prisms, it was found that the two accessible crystalline plane rotations were proportional to each other (see also the experimental diffraction pattern distributions shown in the Supplemental Information, which are all elongated in the plane perpendicular to the Bragg vector, *i. e.*, the (q_2, q_3) plane). Hence, the lattice orientation was expressed directly with respect to the reduced coordinate δ, which measures the crystal rotation around the axis perpendicular to the intensity distribution plane.

References

1. Weiner, S. & Addadi, L. Design strategies in mineralized biological materials. *J. Mater. Chem.* **7,** 689–702 (1997).
2. Boggild, O. M. The shell structure of molluscs. *Kgl Dan. Vidensk Selsk Skr Natruvidensk Og Mathem* **2,** 231–236 (1930).
3. Grégoire, C. Structure of molluscan shell. in *Mollusca* (eds. Florkin, M. & Scheer, B. T.) **VII,** 45–145 (Academic press, 1972).
4. Taylor, J. D. & Kennedy, W. J. The shell structure and mineralogy of the Bivalvia : introduction, nuculacea-trigonacea. *Bull. Br. Mus. Nat. Hist.* **3,** 1–125 (1969).
5. Cuif, J.-P. *et al.* Evidence of a Biological Control over Origin, Growth and End of the Calcite Prisms in the Shells of Pinctada margaritifera (Pelecypod, Pterioidea). *Minerals* **4,** 815–834 (2014).
6. Farre, B. *et al.* Shell layers of the black-lip pearl oyster Pinctada margaritifera: Matching microstructure and composition. *Comp. Biochem. Physiol. B Biochem. Mol. Biol.* **159,** 131–139 (2011).
7. Dauphin, Y. *et al.* Structure and composition of the nacre–prisms transition in the shell of Pinctada margaritifera (Mollusca, Bivalvia). *Anal Bioanal Chem* **390,** 1659–1669 (2008).
8. Dauphin, Y. The nanostructural unity of Mollusc shells. *Mineral. Mag.* **72,** 243–246 (2008).
9. Sethmann, I., Hinrichs, R., Wörheide, G. & Putnis, A. Nano-cluster composite structure of calcitic sponge spicules—A case study of basic characteristics of biominerals. *J. Inorg. Biochem.* **100,** 88–96 (2006).
10. Baronnet, A., Cuif, J. P., Dauphin, Y., Farre, B. & Nouet, J. Crystallization of biogenic Ca-carbonate within organo-mineral micro-domains. Structure of the calcite prisms of the Pelecypod Pinctada margaritifera (Mollusca) at the submicron to nanometre ranges. *Mineral. Mag.* **72,** 617–626 (2008).
11. Dauphin, Y. Soluble Organic Matrices of the Calcitic Prismatic Shell Layers of Two Pteriomorphid Bivalves Pinna nobilis and Pinctada margaritifera. *J. Biol. Chem.* **278,** 15168–15177 (2003).
12. Jacob, D. E. *et al.* Nanostructure, composition and mechanisms of bivalve shell

growth. *Geochim. Cosmochim. Acta* **72,** 5401–5415 (2008).
13. Cölfen, H. & Antonietti, M. Mesocrystals: Inorganic Superstructures Made by Highly Parallel Crystallization and Controlled Alignment. *Angew. Chem. Int. Ed.* **44,** 5576–5591 (2005).
14. Berman, A. *et al.* Biological control of crystal texture: a widespread strategy for adapting crystal properties to function. *Science* **259,** 776–779 (1993).
15. Gilow, C., Zolotoyabko, E., Paris, O., Fratzl, P. & Aichmayer, B. Nanostructure of Biogenic Calcite Crystals: A View by Small-Angle X-Ray Scattering. *Cryst. Growth Des.* **11,** 2054–2058 (2011).
16. Pokroy, B. *et al.* Anisotropic lattice distortions in biogenic calcite induced by intra-crystalline organic molecules. *J. Struct. Biol.* **155,** 96–103 (2006).
17. Pokroy, B., Fitch, A. & Zolotoyabko, E. The Microstructure of Biogenic Calcite: A View by High-Resolution Synchrotron Powder Diffraction. *Adv. Mater.* **18,** 2363–2368 (2006).
18. Okumura, T., Suzuki, M., Nagasawa, H. & Kogure, T. Microstructural Variation of Biogenic Calcite with Intracrystalline Organic Macromolecules. *Cryst. Growth Des.* **12,** 224–230 (2012).
19. Okumura, T., Suzuki, M., Nagasawa, H. & Kogure, T. Characteristics of biogenic calcite in the prismatic layer of a pearl oyster, Pinctada fucata. *Micron* **41,** 821–826 (2010).
20. Gilbert, P. U. P. A., Young, A. & Coppersmith, S. N. Measurement of c-axis angular orientation in calcite (CaCO3) nanocrystals using X-ray absorption spectroscopy. *Proc. Natl. Acad. Sci.* **108,** 11350–11355 (2011).
21. Olson, I. C. *et al.* Crystal lattice tilting in prismatic calcite. *J. Struct. Biol.* **183,** 180–190 (2013).
22. Berman, A. *et al.* Intercalation of Sea Urchin Proteins in Calcite: Study of a Crystalline Composite Material. *Science* **250,** 664–667 (1990).
23. Sayre, D. Some implications of a theorem due to Shannon. *Acta Crystallogr.* **5,** 843–843 (1952).
24. Miao, J., Charalambous, P., Kirz, J. & Sayre, D. Extending the methodology of X-ray crystallography to allow imaging of micrometre-sized non-crystalline specimens. *Nature* **400,** 342–344 (1999).
25. Miao, J., Ishikawa, T., Robinson, I. K. & Murnane, M. M. Beyond crystallography: Diffractive imaging using coherent x-ray light sources. *Science* **348,** 530–535 (2015).
26. Ayyer, K. *et al.* Macromolecular diffractive imaging using imperfect crystals. *Nature* **530,** 202–206 (2016).
27. Büttner, F. *et al.* Dynamics and inertia of skyrmionic spin structures. *Nat. Phys.* **11,** 225–228 (2015).
28. Ulvestad, A. *et al.* Topological defect dynamics in operando battery nanoparticles. *Science* **348,** 1344–1347 (2015).
29. Chamard, V. *et al.* Three-Dimensional X-Ray Fourier Transform Holography: The Bragg Case. *Phys. Rev. Lett.* **104,** 165501 (2010).
30. Rodenburg, J. M. & Bates, R. H. T. The Theory of Super-Resolution Electron Microscopy Via Wigner-Distribution Deconvolution. *Philos. Trans. R. Soc. Lond. Math. Phys. Eng. Sci.* **339,** 521–553 (1992).
31. Pfeifer, M. A., Williams, G. J., Vartanyants, I. A., Harder, R. & Robinson, I. K. Three-dimensional mapping of a deformation field inside a nanocrystal. *Nature* **442,** 63–66 (2006).
32. Dierolf, M. *et al.* Ptychographic X-ray computed tomography at the nanoscale. *Nature* **467,** 436–439 (2010).
33. Rodenburg, J. M. *et al.* Hard-X-Ray Lensless Imaging of Extended Objects. *Phys. Rev. Lett.* **98,** 34801 (2007).

34. Godard, P. *et al.* Three-dimensional high-resolution quantitative microscopy of extended crystals. *Nat. Commun.* **2,** 568 (2011).
35. Berenguer, F. *et al.* X-ray lensless microscopy from undersampled diffraction intensities. *Phys. Rev. B* **88,** 144101 (2013).
36. Pateras, A. I. *et al.* Nondestructive three-dimensional imaging of crystal strain and rotations in an extended bonded semiconductor heterostructure. *Phys. Rev. B* **92,** 205305 (2015).
37. Birkbak, M. E., Guizar-Sicairos, M., Holler, M. & Birkedal, H. Internal structure of sponge glass fiber revealed by ptychographic nanotomography. *J. Struct. Biol.* **194,** 124–128 (2016).
38. Holt, M. V. *et al.* Strain Imaging of Nanoscale Semiconductor Heterostructures with X-Ray Bragg Projection Ptychography. *Phys. Rev. Lett.* **112,** 165502 (2014).
39. Checa, A. G. *et al.* Crystallographic orientation inhomogeneity and crystal splitting in biogenic calcite. *J. R. Soc. Interface* **10,** 20130425 (2013).
40. Godard, P., Allain, M., Chamard, V. & Rodenburg, J. Noise models for low counting rate coherent diffraction imaging. *Opt. Express* **20,** 25914 (2012).
41. Takagi, S. A Dynamical Theory of Diffraction for a Distorted Crystal. *J. Phys. Soc. Jpn.* **26,** 1239 (1969).
42. Hruszkewycz, S. O. *et al.* High-resolution three-dimensional structural microscopy by single-angle Bragg ptychography. *Nat. Mater.* **16,** 244–251 (2017).
43. Nouet, J., Baronnet, A. & Howard, L. Crystallization in organo-mineral micro-domains in the crossed-lamellar layer of Nerita undata (Gastropoda, Neritopsina). *Micron* **43,** 456–462 (2012).
44. Cuif, J. P. & Dauphin, Y. The Environment Recording Unit in coral skeletons – a synthesis of structural and chemical evidences for a biochemically driven, stepping-growth process in fibres. *Biogeosciences* **2,** 61–73 (2005).
45. Bayerlein, B. *et al.* Self-similar mesostructure evolution of the growing mollusc shell reminiscent of thermodynamically driven grain growth. *Nat. Mater.* **13,** 1102–1107 (2014).
46. Gower, L. B. Biomimetic Model Systems for Investigating the Amorphous Precursor Pathway and Its Role in Biomineralization. *Chem. Rev.* **108,** 4551–4627 (2008).
47. Xu, A.-W., Ma, Y. & Cölfen, H. Biomimetic mineralization. *J. Mater. Chem.* **17,** 415–449 (2007).
48. Frølich, S. *et al.* Smaller Calcite Lattice Deformation Caused by Occluded Organic Material in Coccoliths than in Mollusk Shell. *Cryst. Growth Des.* **15,** 2761–2767 (2015).
49. Li, H., Xin, H. L., Muller, D. A. & Estroff, L. A. Visualizing the 3D Internal Structure of Calcite Single Crystals Grown in Agarose Hydrogels. *Science* **326,** 1244–1247 (2009).
50. Meldrum, F. C. & Coelfen, H. Crystallization and formation mechanisms of nanostructures. *Nanoscale* **2,** 2326–2327 (2010).
51. Nudelman, F., Chen, H. H., Goldberg, H. A., Weiner, S. & Addadi, L. Spiers Memorial Lecture. *Faraday Discuss.* **136,** 9–25 (2007).
52. Addadi, L., Moradian, J., Shay, E., Maroudas, N. G. & Weiner, S. A chemical model for the cooperation of sulfates and carboxylates in calcite crystal nucleation: Relevance to biomineralization. *Proc. Natl. Acad. Sci.* **84,** 2732–2736 (1987).
53. Gower, L. B. & Odon, D. J. Deposition of calcium carbonate films by a polymer-induced liquid-precursor (PILP) process. *J. Cryst. Growth* **210,** 719–734 (2000).
54. Bewernitz, M. A., Gebauer, D., Long, J., Cölfen, H. & Gower, L. B. A metastable liquid precursor phase of calcium carbonate and its interactions with polyaspartate. *Faraday Discuss.* **159,** 291–312 (2012).

Supplemental Figures 1 to 8 are provided as Supplementary Information.

Acknowledgments: Y. Dauphin and J.-P. Cuif are warmly acknowledged for their invaluable inputs to the research program. G. Le Moullac (IFREMER) is acknowledged for giving access to the shell samples. J. Savatier is warmly acknowledged for his help during the optical microscopy imaging session. We acknowledge the ESRF for providing access to the source. This work was funded by the French ANR under project number ANR-11-BS20-0005 and it has received funding from the European Research Council (ERC) under the European Union's Horizon H2020 research and innovation program grant agreement No 724881. Additional supports were received from Aix-Marseille University A*Midex (ANR-11-IDEX-0001-02), ANR grants France Bio Imaging (ANR-10-INSB-04-01) and France Life Imaging (ANR-11-INSB- 0006).

Author Contributions

VC, JDa and MB conceived the experiment with contributions from PGo, CC and PGu. PGo, MA and VC developed the inversion code. VC, MB, PGo, CC and JDa performed the experiments at ID13, ESRF. The 3D ptychography reconstructions were performed by FM with inputs and discussion from VC and PGo. JDu performed the white light microscopy experiment and performed and analyzed the CARS experiments. JNo performed the AFM experiments. FM, VC, JDa, CC and JNo wrote the manuscript with contributions from all co-authors.

Author Information

The authors declare no competing financial interest.

Correspondence

Correspondence should be sent to V. Chamard, virginie.chamard@fresnel.fr.

Code availability

Matlab routines for 3D Bragg ptychography reconstruction from an experimental data set are available on demand by contacting the corresponding author.

Data availability statement

The experimental data that support the plots within this paper are available on demand by contacting the corresponding authors.

Figures

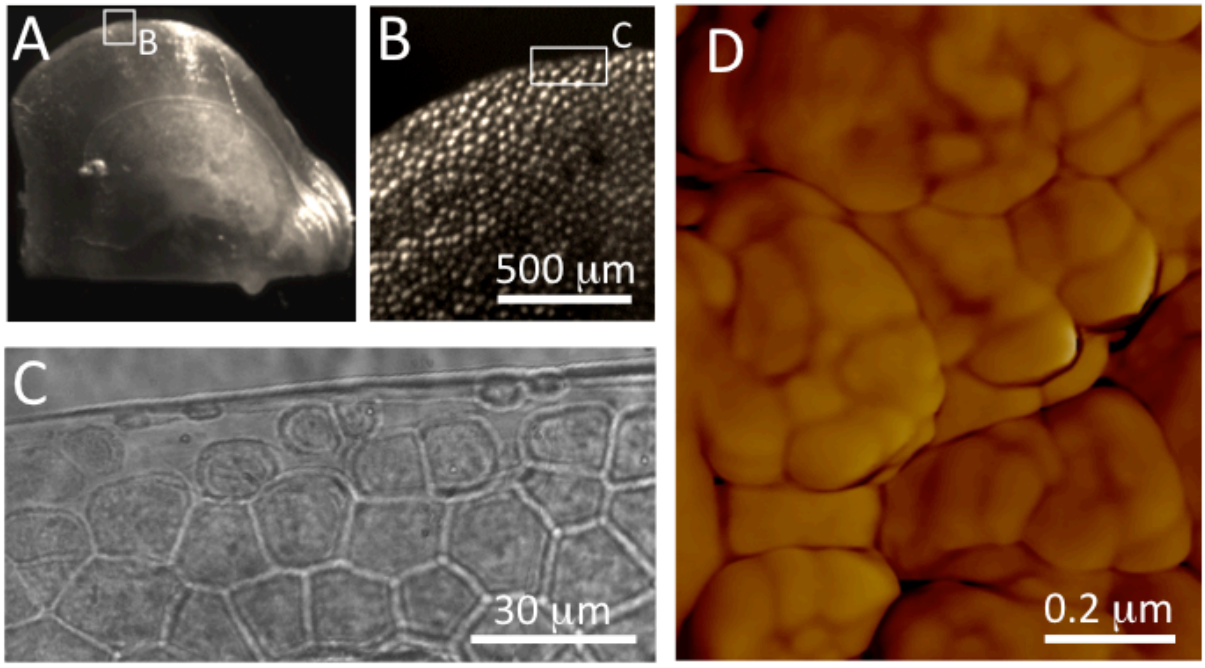

Fig. 1: Structure of *Pinctada margaritifera* shell at different length scales. (A-C) Optical micrographs of a juvenile *Pinctada margaritifera*. (A) The whole shell. (B) Zoom-in view showing the prism assembly in the vicinity of the growth border. (C) The shell growth border. One clearly identifies calcite prisms, delimited by thick organic walls, as well as isolated disks, the preliminary form of the prisms. (D) Atomic force microscopy images (phase contrast) obtained on the surface of a *Pinctada margaritifera* prism showing the granule assembly, a common structure of many calcifying organisms.

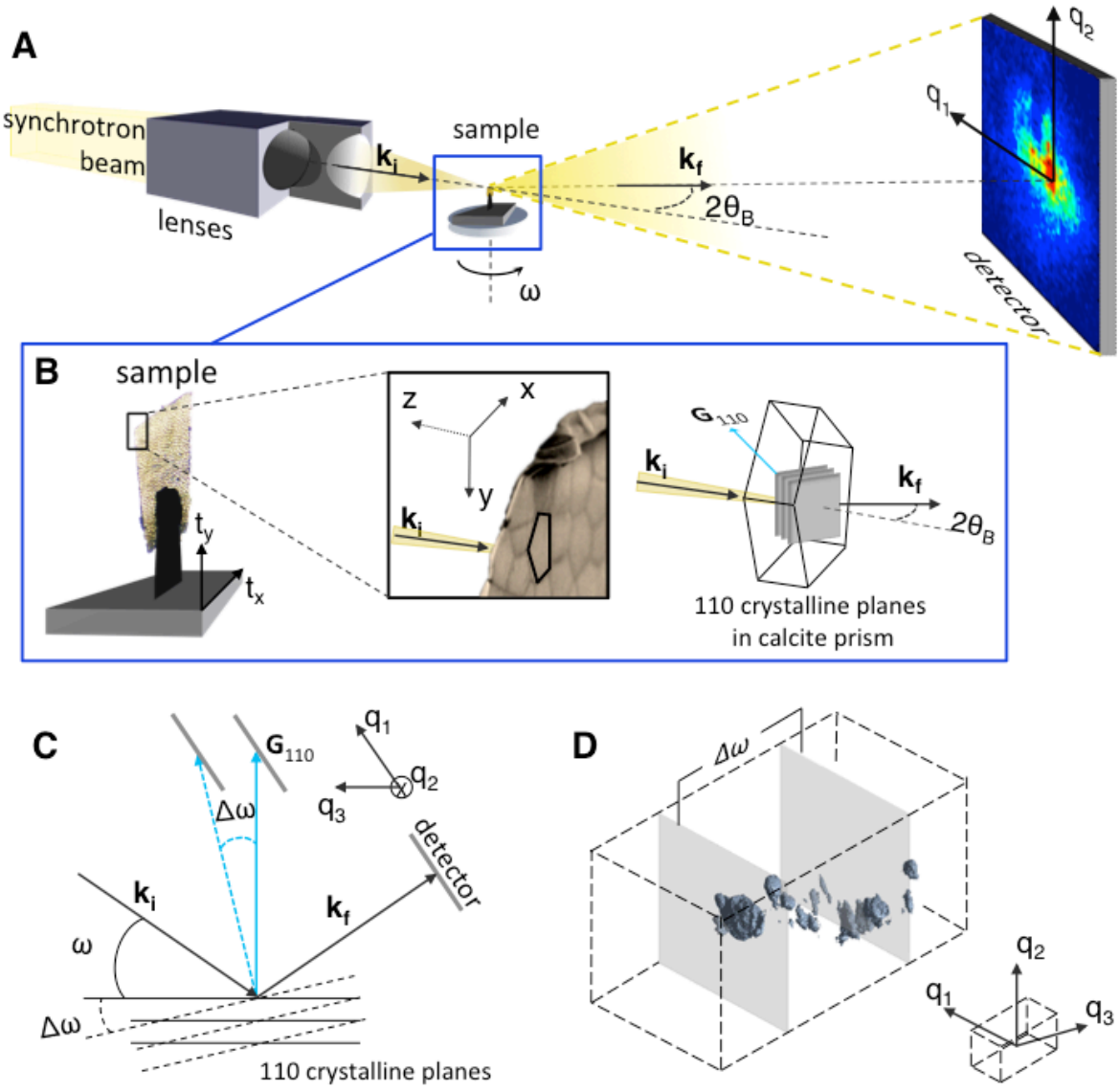

Fig. 2: 3D Bragg diffraction ptychography set-up. (A) The sample is placed in the focus of a coherent x-ray nano-beam and oriented in Bragg diffraction condition in Laue geometry. The far-field intensity patterns are collected by a 2D detector. (B) (*left*) Details of the sample positioning together with the ptychographic translations (t_x and t_y), whose spatial displacements cover the region of interest. (*middle*) Zoom-in view of the sample where the selected prism is highlighted. The shell thickness is about 1 μm at the border. The (**x**,**y**,**z**) orthogonal laboratory frame is related to the sample, with x- and y-axes along the surface of the prism and z-axis along the growth direction of the prism. The t_x and t_y ptychography scanning directions are collinear and anti-collinear to the x-and y-axes, respectively. (*right*) Chosen 110 Bragg reflection with respect to the prism. The G110 Bragg vector lies in the (**x**,**z**) plane. (C) Successive acquisitions of 2D diffraction patterns, obtained by scanning the sample along the incidence angle ω in steps of δω, result in the exploration of the 3D intensity distribution arising from the chosen crystalline family planes. The intensity is registered as a function of $\mathbf{q} = \mathbf{k}_f - \mathbf{k}_i$, in the 3D detection frame ($\mathbf{q}_1$, $\mathbf{q}_2$, $\mathbf{q}_3$). (D) Schematic view of the 3D detection frame and iso-surface rendition of the 3D intensity distribution integrated over all illumination positions. Two detection planes, separated by n steps along the ω scan, are shown in grey.

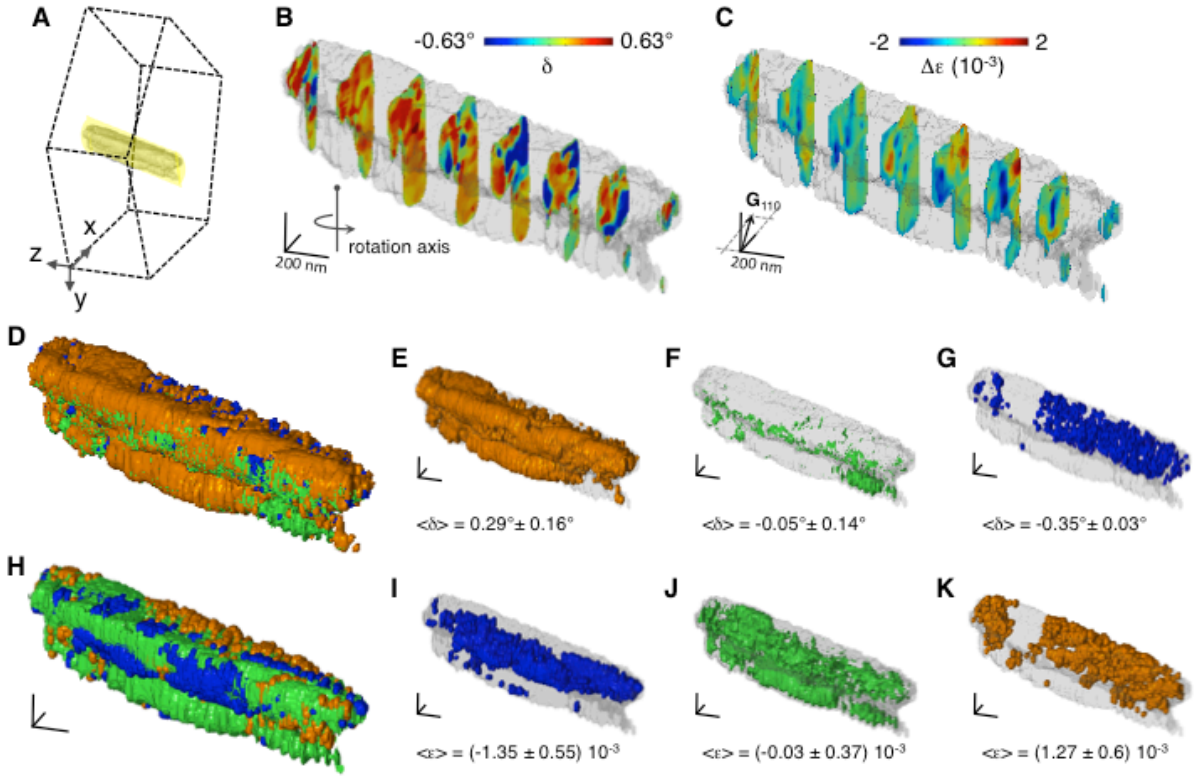

Fig. 3. 3D Bragg ptychography reconstruction. (A) Schematic view of the reconstructed volume within the prism (in yellow-gray), embedded into the probed region (yellow cylinder). (B) and (C) Crystalline rotation (δ) and relative strain (ε) variation maps shown on several planes along the reconstructed volume, corresponding respectively to the rotation of the (110) crystalline planes around the rotation axis shown in (B) and to the relative crystalline displacement along $\mathbf{G}_{110}$. Iso-oriented and iso-strain regions, *i. e.*, regions presenting the same rotation or strain value, are evidenced. (D) Same as (B) shown as an isosurface rendering (with respect to δ values) of all iso-oriented crystalline domains. The colors encode the respective rotation angles δ according to the color-scale in (B). The total retrieved volume corresponds to the one shown in A. (E-G) Single iso-oriented crystalline domains, for three rotation angles δ indicated in the figure. (H) Same as (C) shown as an isosurface rendering (with respect to ε values) of all iso-strain domains. (I-K) Single iso-strain domains, for three relative strain ε indicated in the figure. The length scale is indicated in (B-K) and represents 200 nm.

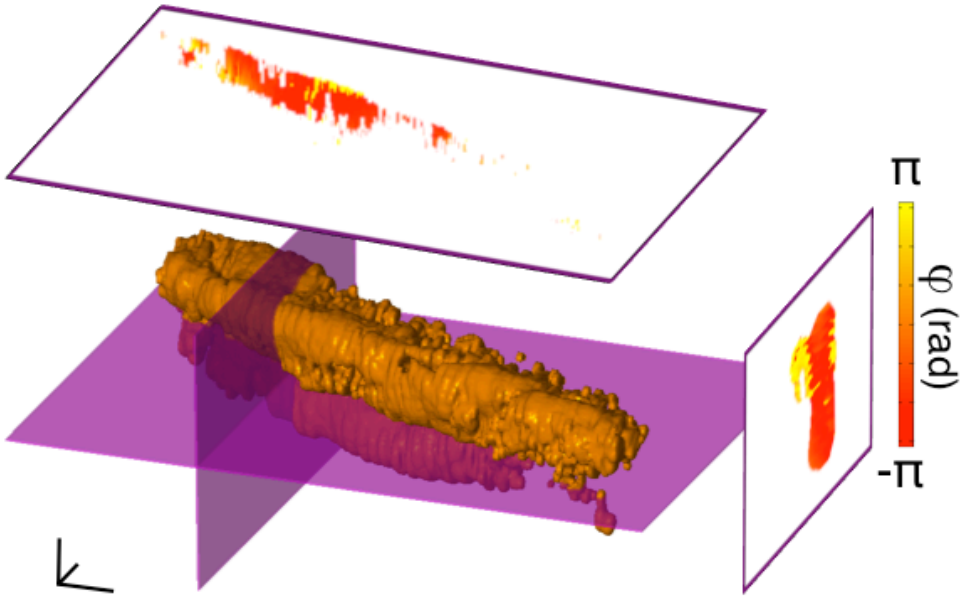

643

644 **Fig. 4: Crystalline coherence in the iso-oriented domain.** 2D cuts of the retrieved phase
645 map φ extracted for the iso-oriented domain of Fig. 3E. This quantity is related to the
646 crystalline coherence: abrupt changes in the phase value correspond to breakdown of the
647 crystalline continuity. In average, the phase shift is about 4.2 radians, corresponding to a
648 displacement of about 0.16 nm, *i. e.* ≈ 2/3 of the (110) lattice spacing. The indicated length
649 scale represents 200 nm.

650